Received: 19 December 2024 | Revised: 4 February 2025 | Accepted: 13 February 2025

DOI: 10.1002/pro.70085

RESEARCH ARTICLE

THE PROTEIN SOCIETY WILEY

A conserved motif in *Henipavirus* P/V/W proteins drives the fibrillation of the W protein from Hendra virus

Frank Gondelaud[1] | **Christophe Bignon**[1] | **Denis Ptchelkine**[1] | **Frédéric Carrière**[2] | **Sonia Longhi**[1]

[1]Laboratoire Architecture et Fonction des Macromolécules Biologiques (AFMB), UMR 7257, Aix Marseille University and Centre National de la Recherche Scientifique (CNRS), Marseille, France

[2]Aix Marseille Univ, CNRS, UMR7281 Bioénergétique et Ingénierie des Protéines, Marseille, France

Correspondence
Frank Gondelaud and Sonia Longhi, Laboratoire Architecture et Fonction des Macromolécules Biologiques (AFMB), UMR 7257, Aix Marseille University and Centre National de la Recherche Scientifique (CNRS), 163 Avenue de Luminy, Case 932, 13288 Marseille, France.
Email: frank.gondelaud@univ-amu.fr; sonia.longhi@univ-amu.fr

Funding information
Agence Nationale de la Recherche, Grant/Award Numbers: ANR-10-INSB- 0005, ANR-21-CE11- 0012-01; Fondation pour la Recherche Médicale, Grant/Award Number: MND202310017898

Review Editor: Jean Baum

Abstract

The Hendra (HeV) and Nipah (NiV) viruses are high-priority, biosafety level-4 pathogens that cause fatal neurological and respiratory disease. Their P gene encodes not only the P protein, an essential polymerase cofactor, but also the virulence factors V and W. We previously showed that the W protein of HeV (W^{HeV}) forms amyloid-like fibrils and that one of its subdomains, PNT3, fibrillates in isolation. However, the fibrillation kinetics is much faster in the case of the full-length W^{HeV} compared to PNT3, suggesting that another W^{HeV} region contributes to the fibrillation process. In this work, we identified the region spanning residues 2–110 (PNT1) as the crucial region implicated in W^{HeV} fibrillation. Through site-directed mutagenesis, combined with thioflavin T binding experiments and negative-staining transmission electron microscopy, we showed that a predicted cryptic amyloidogenic region (CAR) within PNT1 is the main driver of fibrillation and deciphered the underlying molecular mechanism. Using FTIR, we showed that PNT1 fibrils are enriched in cross β-sheets. Sequence alignment revealed conservation of the CAR across the *Henipavirus* genus and enabled the identification of a hitherto never reported pro-amyloidogenic motif. The ability to form fibrils was experimentally shown to be a common property shared by *Henipavirus* PNT1 proteins. Overall, this study sheds light on the molecular mechanisms underlying W^{HeV} fibrillation and calls for future studies aimed at exploring the relevance of the newly identified pro-amyloidogenic motif as a valuable target for antiviral approaches.

KEYWORDS
amyloidogenic regions and motifs, circular dichroism, fibrillation mechanisms, FTIR spectroscopy, negative-staining transmission electron microscopy, thioflavin T binding

1 | INTRODUCTION

The Hendra (HeV) and Nipah (NiV) viruses are deadly zoonotic pathogens belonging to the *Paramyxoviridae* family of the *Mononegavirales* order, classified among high-priority targets by the WHO. The absence of therapeutics, their extremely high case fatality rate (70%–100%), and their pandemic potential bring both HeV and NiV into the biosafety-level 4 category (Gazal et al. 2022; Li et al. 2023). They are responsible for annual outbreaks in Asia and Australia, causing severe neurological and respiratory illness (Kaza and Aguilar 2023; Li et al. 2023). Both viruses are hosted by fruit bats of the *Pteropus* genus, and the transmission to humans is made through the consumption of infected raw date palm sap or through close contact with

infected pigs and horses (Kaza and Aguilar 2023). The Henipavirus genus keeps growing with the novel identification of Langya virus (LayV) in China (Isaacs et al. 2023; Piracha et al. 2023) and of the Angavokely virus (AngV) in Madagascar (Madera et al. 2022).

Henipaviruses are enveloped viruses containing a non-segmented single-stranded RNA genome of negative polarity. The P gene encodes the phosphoprotein (P) that ensures viral replication in association with the RNA-dependent RNA polymerase (L). In henipaviruses, the P gene often also encodes the C, V, and W proteins: while C results from an alternative reading frame, V and W are generated through a mechanism involving the addition of one (V) or two (W) non-templated guanosine nucleotides at the editing site of the P messenger (Quarleri et al. 2022). Consequently, P, V, and W share a large N-terminal domain (NTD), while their C-terminal domain (CTD) differs. The NTD from NiV and HeV is intrinsically disordered (Habchi et al. 2010; Jensen et al. 2020; Schiavina et al. 2020), as are the full-length W proteins (Pesce et al. 2022) and their respective CTDs (Pesce et al. 2024). By contrast, the CTD of the V protein consists of a zinc-finger domain (Salladini et al. 2017). While V is cytosolic, W is internalized in the nucleus of infected cells via several importins due to the presence of a nuclear localization sequence (NLS) present in its unique CTD (Smith et al. 2018). Although the NTD common to P, V, and W is intrinsically disordered, it contains an N-terminal α-MoRE, that is, a disordered binding site that folds into an α-helix upon binding to a protein partner. This region extends up to 35 amino acids and is responsible for the binding of P to the monomeric form of the nucleoprotein (N°) thereby inhibiting N self-polymerization (Yabukarski et al. 2014).

V and W are the main virulence factors, and they do so by interfering with the antiviral response (Kaza and Aguilar 2023; Basler 2012; Keiffer et al. 2020). In particular, they both bind and sequester STAT proteins among other key cell proteins involved in the host innate immune response (see Audsley and Moseley 2013; Gondelaud et al. 2022 for review).

We previously showed that the NiV and HeV W proteins are able to form amyloid-like fibrils *in vitro* and *in cellula* (Gondelaud et al. 2024; Pesce et al. 2022; Pesce et al. 2024), although their biological function has not been elucidated so far and is only hypothesized (Escudero-Pérez et al. 2023; Gondelaud et al. 2022; Gondelaud et al. 2023). Fibrillation, however, only occurs after a pre-incubation period in oxidative conditions during which disulfide-bridged dimers, which are critical for nucleation, are formed (Gondelaud et al. 2024). In the absence of such an oxidative pre-incubation, NiV and HeV W only form insoluble and amorphous aggregates (Gondelaud et al. 2024).

The PNT3 region (residues 200–310), common to the P, V, and W proteins, was found to be able to fibrillate (Nilsson et al. 2022; Salladini et al. 2021). However, while the full-length W protein fibrillates in a few hours (Gondelaud et al. 2024; Pesce et al. 2022), the fibrillation of isolated PNT3 domain requires a much longer incubation time and higher protein concentration (Nilsson et al. 2022). These differences in the fibrillation kinetics suggest that other W regions contribute to W^{HeV} fibrillation. To answer this question, we used a domain approach and performed biophysical analysis on isolated W^{HeV} fragments. Since previous studies showed that the CTD of W^{HeV} is devoid of intrinsic fibrillogenic properties (Pesce et al. 2024), we focused on the W^{HeV} NTD and performed biophysical analyses on its isolated NTD subdomains. We found that the PNT1 region (residues 1–110) is the main driver of W^{HeV} fibrillation. We identified the crucial region, and residues thereof, implicated in PNT1 fibrillation and showed that adjacent fluctuating α-helices play a critical role in the nucleation step. Finally, we show that the PNT1 region of the P/V/W proteins from other henipaviruses is also able to fibrillate, pointing to a new common molecular property shared by members of the *Henipavirus* genus.

2 | RESULTS

2.1 | Inducing α-helical folding promotes W^{HeV} and W^{NiV} fibrillation

Although W^{HeV} and W^{NiV} are predicted to be entirely disordered by the MFDp disorder metapredictor (Mizianty et al. 2010) (Figure S1a), and effectively experimentally shown to be disordered (Habchi et al. 2010; Jensen et al. 2020; Schiavina et al. 2020), they contain residual α-helical elements in their NTD (Jensen et al. 2020; Schiavina et al. 2020; Yabukarski et al. 2014). In particular, these are located within the first 50 residues known to interact with the unassembled form of the nucleoprotein (N°) (Yabukarski et al. 2014), and in the region encompassing residues 340–355 (Jensen et al. 2020; Schiavina et al. 2020) that possibly corresponds to a putative additional weak binding site for the nucleoprotein by analogy with measles virus (Milles et al. 2018). Interestingly, these (putative) α-MoREs coincide with drops in the disorder profiles of the W proteins (Figure S1a). We addressed the question as to whether these transiently populated α-helices could play a role in the fibrillation process. We thus incubated the W proteins with low concentrations of the secondary structure stabilizer 2,2,2-trifluoroethanol (TFE) and monitored their aggregation propensity by means of turbidity and thioflavin T (ThT) fluorescence measurements (Figure 1a,b). For this purpose, reduced proteins were used, a condition where fibrils should not be able to form (Gondelaud et al. 2024). Following the addition of 5% or 10% (v/v)

TFE, turbidity measurements showed a reduced solubility for W^{HeV} with no clear dependence on TFE concentration, while W^{NiV} was not affected (Figure 1a). However, a gradual increase in ThT binding was observed for both proteins, suggesting the formation of amyloid-like fibrils in a TFE concentration-dependent manner (Figure 1b). A TFE concentration as low as 5% was found to be sufficient to promote a weak, though detectable, increase in the α-helical content in both W^{HeV} and W^{NiV}, as shown by far-UV circular dichroism (CD) experiments (Figure 1c,d). In the presence of 10% TFE, a further increase in the α-helical content is observed, this being particularly pronounced in the case of W^{NiV} (Figure 1c,d). Negative-staining transmission electron microscopy (NS-TEM) studies showed that 5% TFE is sufficient to trigger the fibrillation of both W^{HeV} and W^{NiV}, suggesting a relation between α-helical content and fibril nucleation (Figure 1e). Additionally, the presence of TFE induces the formation of significant amounts of circular fibrils, suggesting that the α-helical content influences their curvature. To the best of our knowledge, the only reported case of circular fibrils concerns insulin when subjected to high hydrostatic pressure (Jansen et al. 2004).

Experimental evidence gathered in recent years indicates that fibrils can result from a "maturation" process of liquid condensates formed through liquid–liquid phase separation (LLPS) (Alberti and Hyman 2021; Gondelaud et al. 2023). LLPS underlies not only the formation of membrane-less organelles (MLOs) but also of viral factories (i.e., replication compartments) in a number of viral families including *Paramyxoviridae* (Brocca et al. 2020; Glon et al. 2024). We thus sought to analyse the LLPS propensities of the W proteins and

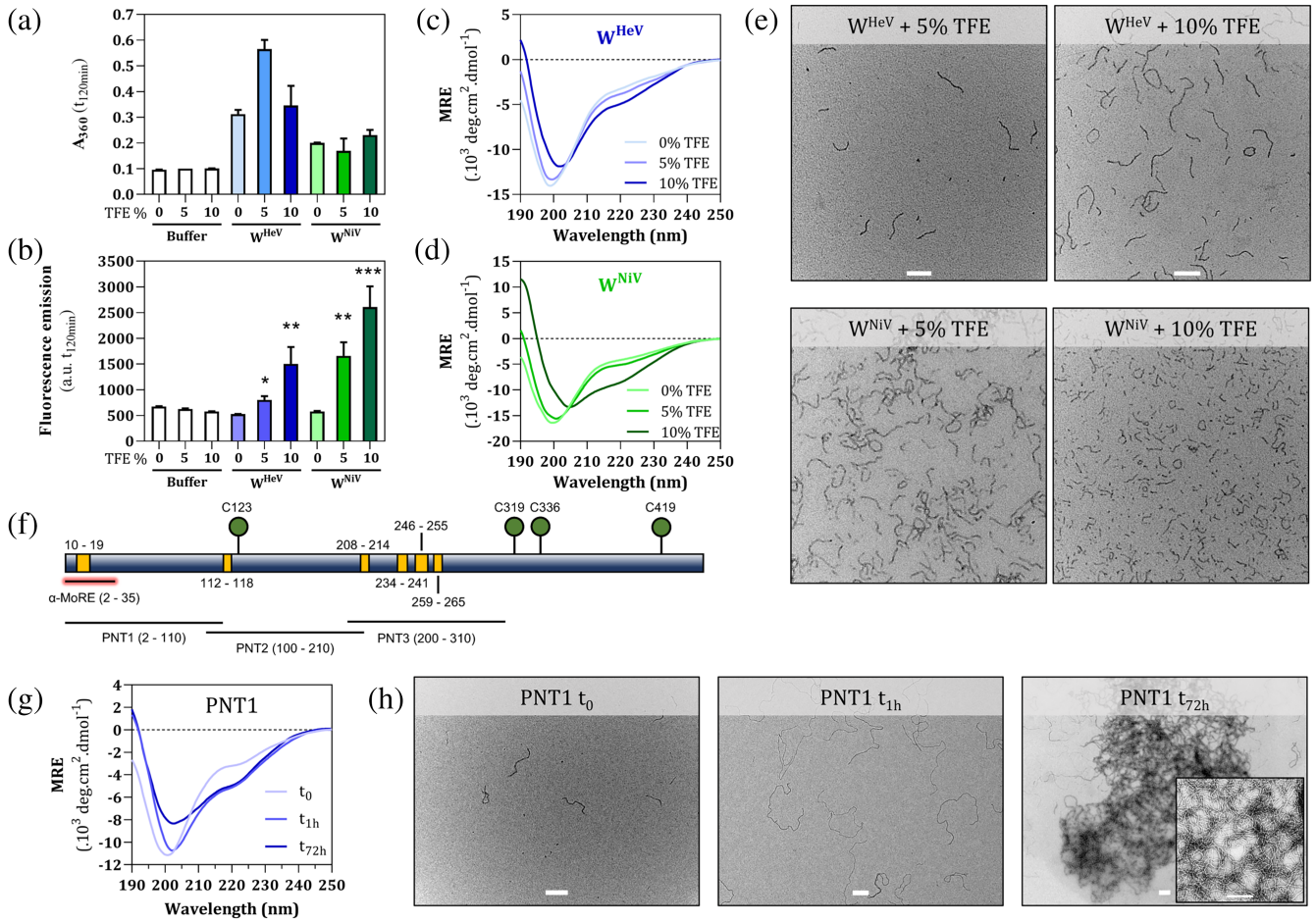

FIGURE 1 PNT1 drives W^{HeV} fibrillation through a mechanism involving α-helices. Turbidity (a) and ThT fluorescence measurements (b) of W^{HeV} and W^{NiV} in the absence or presence of 5% or 10% (v/v) TFE after 120 min of incubation and without a pre-incubation in oxidative conditions ($n = 4$). Asterisks above error bars denote significance compared to the protein-free conditions. *$p < 0.05$, **$p < 0.01$, ***$p < 0.0001$. Circular dichroism (CD) spectra of W^{HeV} (c) and W^{NiV} (d) in the absence or presence of 5% or 10% (v/v) TFE. MRE, mean residue ellipticity. (e) NS-TEM observations of W^{HeV} and W^{NiV} in the absence or presence of 5% or 10% (v/v) TFE after 120 min of incubation. Scale bar: 200 nm. (f) Schematic representation of W^{HeV} (blue) with its predicted amyloid hotspots (orange boxes) and cysteine residues (green circles). PNT1, PNT2, and PNT3 subdomains and the α-MoRE are indicated. (g) Near-UV spectra as obtained during CD experiments of W^{HeV} PNT1 unincubated (t_0) or incubated for 1 h or 72 h without TFE. (h) NS-TEM observations of W^{HeV} PNT1 after 0, 1 h, and 72 h of incubation. Inset: higher magnification at t_{72h} highlighting the fibrillar nature of W^{HeV} PNT1. Scale bar: 200 nm.

of their derived fragments or variants (see below) (Figure S2a,b). Both W proteins are predicted to be phase-separating proteins by the MolPhase predictor (Liang et al. 2024), as judged from their very high LLPS score, with the PNT3 fragment mainly accounting for this propensity (Figure S2a). In the absence of TFE, however, both proteins were found to display a relatively low turbidity (Figure 1a), consistent with the lack of phase-separated droplets. In addition, although we previously reported that PNT3 phase separates in the presence of PEG, FRAP analyses revealed that PNT3 condensates have a solid-like nature (Salladini et al. 2021), and no evidence was obtained so far in favor of a droplet state preceding the formation of fibrils, neither for the *Henipavirus* W proteins nor for any of its fragments and variants generated in this study.

2.2 | W^{HeV} possesses several cryptic amyloidogenic regions, and PNT1 is the most fibrillogenic NTD subdomain

Analysis of the cryptic amyloidogenic region (CAR) database (Pintado-Grima et al. 2022) revealed that W^{HeV} contains six cryptic amyloidogenic regions (CARs) distributed along the NTD (Figure 1f). CARs are regions of mild amyloidogenic potential, yet they are able to assemble into fibrils when in isolation (Pintado-Grima et al. 2022). Interestingly, three out of these CARs (i.e., those encompassing aa 10–19, aa 112–118, and aa 208–214) are also consistently predicted as amyloidogenic by the FoldAmyloid predictor (Garbuzynskiy et al. 2010) (Figure S3a). The sequence comprising residues Ile^{208} to Thr^{265} is particularly enriched in CARs. These latter are located in the PNT3 region (W^{HeV} residues 200–310) that we previously showed to be fibrillogenic (Nilsson et al. 2022; Salladini et al. 2021). We took advantage of the availability in our lab of constructs encoding W^{HeV} PNT1 (residues 2–110), PNT2 (residues 100–210), and PNT3 (residues 200–310) (Salladini et al. 2021), which all contain at least one predicted CAR (Figure 1f), to characterize them individually. For this purpose, each protein region was incubated for 0, 1, and 72 h prior to analysis by CD and NS-TEM (Figures 1g,h and S4a,b).

The far-UV CD spectra of unincubated subdomains display a strong negative peak around 200 nm typical of disordered proteins (Figures 1g and S4a), in agreement with predictions (Figure S1a). Nevertheless, PNT1 exhibits a weak negative peak at around 220 nm, suggesting the presence of residual α-helicity (Figure 1g). Upon incubation, while PNT2 and PNT3 spectra do not evolve significantly (Figure S4a), for PNT1, a gradual change in the 210–230 nm region was observed, indicating the formation of secondary structures (Figure 1g). Micrographs revealed that PNT1 fibrillates immediately after urea removal, while a prolonged incubation (i.e., 72 h) led to a massive tangle of fibrils of micrometric scale (Figure 1h). By contrast, even after a 72-h incubation, rare fibrils were observed in the case of PNT2, and none for PNT3, which was indeed already known to require longer incubation time and higher protein concentrations to fibrillate (Nilsson et al. 2022) (Figure S4b). These results indicate that PNT1 is the most fibrillogenic NTD subdomain, a finding that could not be anticipated by predictions (Figure S3a).

2.3 | The first 50 residues of W^{HeV} are required for fibrillation

The increased fibrillogenicity of the full-length W proteins in the presence of TFE suggests an involvement of transiently populated regular secondary structure elements in the fibrillation process. Because W^{HeV} PNT1 was found to be the most fibrillogenic region and because its NiV counterpart contains a well-characterized α-MoRE at its N-terminal extremity (Yabukarski et al. 2014), we focused on this fragment and generated a HeV PNT1 variant (referred to as 50φPNT1) where the first N-terminal 50 residues were exchanged with an artificial disordered sequence of the same length (Figure 2a). To this end, we used the InSiDDe server (Schramm et al. 2017) and chose a sequence with the same disorder content (as predicted by IUPred2A (Erdős and Dosztányi 2020) and same charge content resulting in a 50φPNT1 construct featuring an isoelectric point (pI) of 4.93, a value close to that of PNT1 (5.0). The resulting sequence is devoid of predicted amyloidogenic regions (Figure S3b) and is predicted to have a higher disorder content (Figure S1b). The far-UV CD spectra of wild-type PNT1 and 50φPNT1 variant were recorded (Figure S5a) and their deconvolution (Figure S5b) enabled inferring their respective secondary structure content and showed, as expected from predictions, an enrichment in disorder and a depletion in α-helices in 50φPNT1 compared to PNT1 (Figure S5a). We also recorded their CD spectra in the presence of increasing amounts of TFE (Figure S5a) and could infer their propensity to undergo an α-helical transition (Figure 2b). As expected, based on the established ability of its α-MoRE to fold into an α-helix (Yabukarski et al. 2014) and on its higher predicted α-helical content (Figure S5c), PNT1 undergoes α-helical folding already at a TFE concentration of 10%, while 50φPNT1 is much less sensitive to TFE (Figures 2b and S5a). NS-TEM analysis of PNT1 and 50φPNT1 samples incubated in the presence or absence of TFE for 30 min at 37°C revealed that while PNT1 fibrillates in the absence of TFE and forms huge fibril clusters in the presence of a TFE concentration as low as 1%, 50φPNT1 is unable to fibrillate even at TFE concentrations as high as 30%

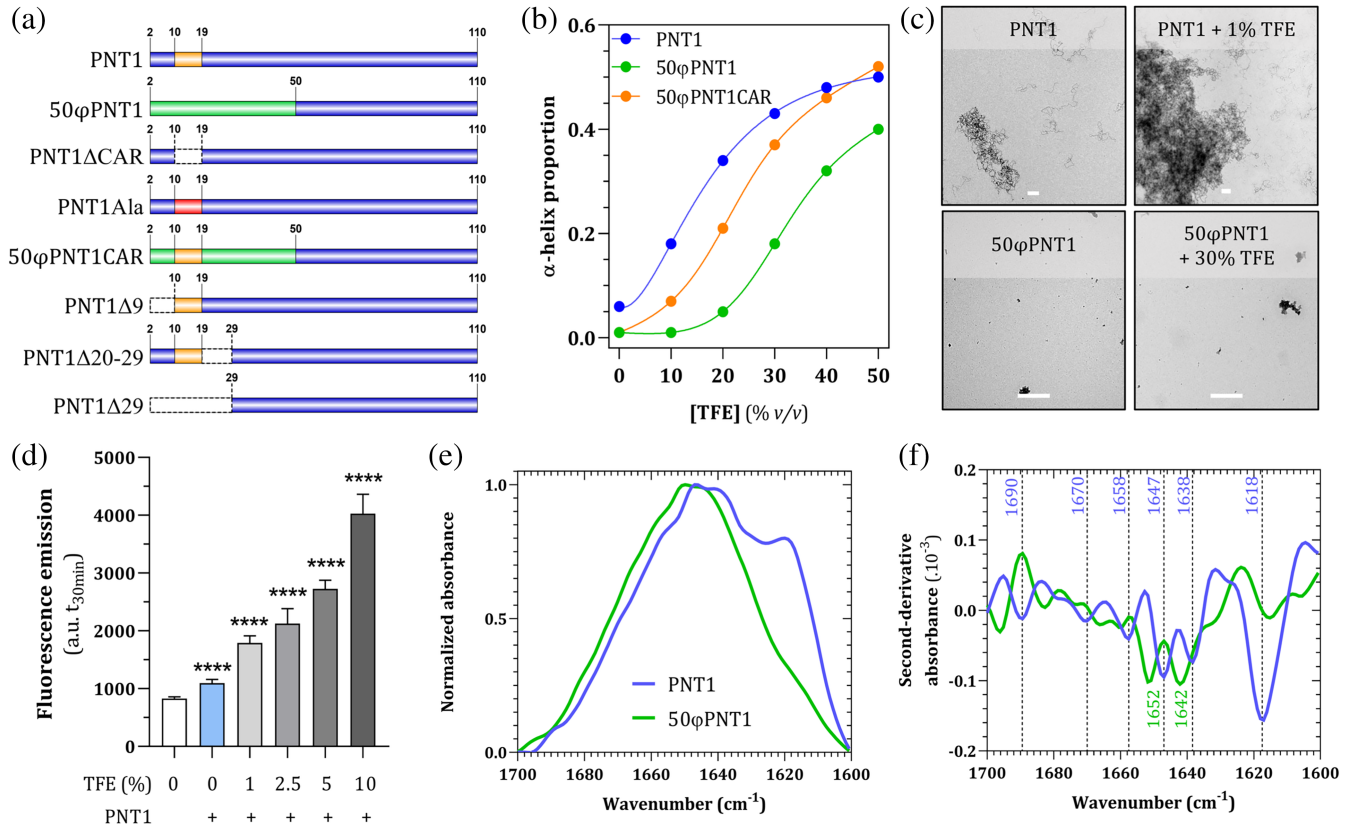

FIGURE 2 The first 50 residues are responsible for W^{HeV} fibrillation and accommodate the cross β-sheet structure observed in fibrils. (a) Schematic representation of the different HeV PNT1 variants generated and used in this work. Orange: CAR motif, green: artificially disordered sequence, red: polyalanine stretch, white: truncated regions. (b) Proportion of α-helix in PNT1, 50φPNT1, and 50φPNT1CAR as obtained from the deconvolution of CD spectra as obtained on unincubated samples. (c) NS-TEM micrographs after 30 min of incubation of PNT1 and 50φPNT1 (both at 40 μM) in the presence of different TFE concentrations. (d) ThT fluorescence measurements of PNT1 in the presence of increasing concentrations of TFE (1–10%) ($n = 12$). Asterisks above error bars denote significance compared to the condition containing only ThT. ****$p < 0.0001$. (e) IR absorption spectra and (f) respective second-derivative IR absorption spectra of PNT1 (blue) and 50φPNT1 (green). Absorption wavenumbers of interest are indicated in blue (PNT1) and green (50φPNT1).

(Figure 2c). These results indicate that the PNT1 amyloidogenic motif is located within the first 50 amino acids, a finding in agreement with the location of the predicted CAR (Figure 1f). ThT binding assays of PNT1 pointed out a gradual increase of fluorescence with increasing TFE concentrations (Figure 2d), mirroring NS-TEM experiments and further underscoring a relationship between α-helical content and fibrillation.

NS-TEM studies showed that the addition of TFE does not trigger fibrillation of PNT2 (Figure S4c), thus underscoring the specific nature of TFE effect on PNT1 fibrils. By contrast, the addition of 5% has a weak, though non-negligible, effect on PNT3, of which it enhances nucleation (Figure S4c). In light of our recent findings showing that PNT3 fibrils are enriched in β structure (Gondelaud et al. 2025), the observed effect of TFE on PNT3 fibrillation likely reflects the ability of TFE to stabilize secondary structure elements. In this regard, we would like to emphasize that TFE is thus a useful tool not only to unveil hidden structural propensities (Receveur-Bréchot et al. 2006; Schramm et al. 2019, and references therein) but also hidden fibrillation propensities.

2.4 | PNT1 fibrils contain cross β-sheets and a small fraction of α-helices

In order to achieve insights into the secondary structure content of PNT1 fibrils, we carried out Fourier-transform infrared spectroscopy (FTIR) analyses. To this end, PNT1 and 50φPNT1 were incubated for 1 h at 37°C, lyophilized, and then deuterated for 48 h at 4°C. Analysis of the Amide I band (1700–1600 cm^{-1}) of the IR spectra of PNT1 and of the non-fibrillating 50φPNT1 variant revealed that both proteins contain disordered regions (1640–1650 cm^{-1}) (Natalello et al. 2012) (Figure 2e,f). The second derivative of the PNT1 spectrum revealed the presence of absorption bands at 1670–1690 cm^{-1}, and especially a pronounced one at 1618 cm^{-1} (Figure 2f). These bands, which are absent in the spectrum of 50φPNT1 (Figure 2f), are all

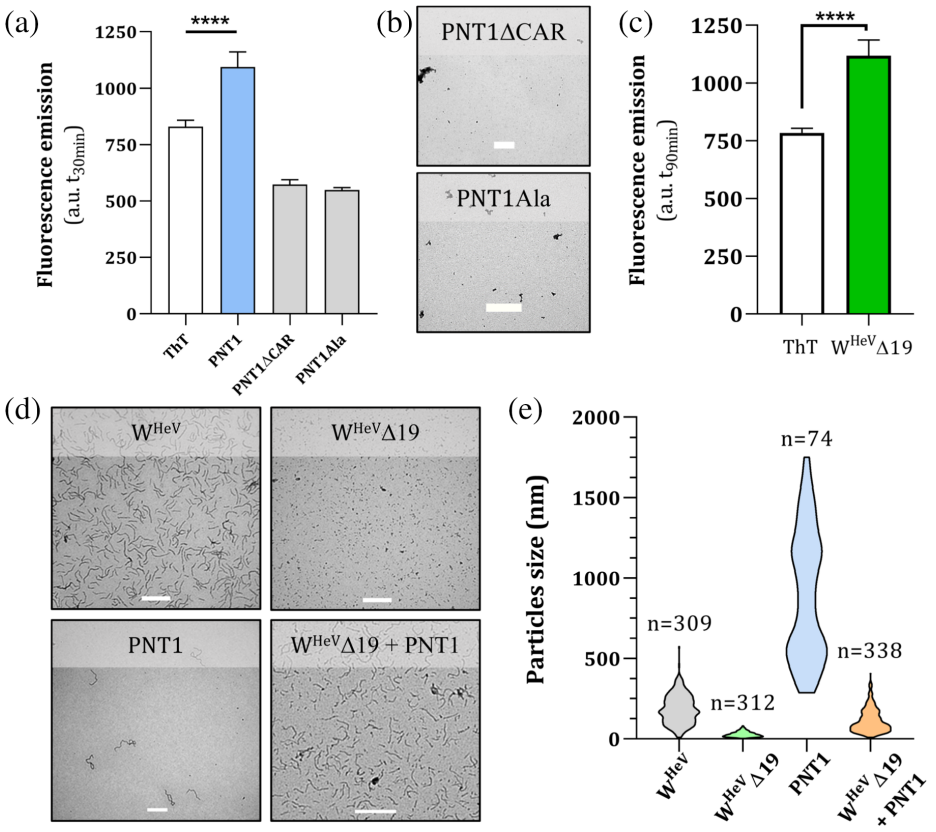

FIGURE 3 A short amyloidogenic motif is responsible for W^{HeV} fibrillation. (a) ThT fluorescence measurements of PNT1, PNT1ΔCAR, and PNT1Ala after 30 min of incubation ($n = 12$). The asterisks denote a statistically significant difference ($p < 0.0001$). (b) Corresponding micrographs after 30 min of incubation of PNT1ΔCAR (top) and PNT1Ala (bottom). Scale bar: 500 nm. (c) ThT fluorescence measurements of W^{HeV} Δ19 after 90 min of incubation ($n = 4$). (d) NS-TEM micrographs as obtained after 90 min of incubation for W^{HeV}, W^{HeV} Δ19 (at 25 μM), PNT1 (25 μM) and of an equimolar mixture of W^{HeV} Δ19 and PNT1 (both at 25 μM). Scale bar: 500 nm. (e) Fibril contour length measurements made on micrographs shown in (d). The number of measurements (n) is indicated.

typical of cross β-sheets, a hallmark of amyloid fibrils. The second derivative of fibrillated PNT1 (Figure 2f) also revealed a small absorption band centered on 1657.5 cm^{-1}, which is typical of α-helices, suggesting that some α-helices are stabilized in fibrils. This band is slightly shifted to 1658.5 cm^{-1} in the 50φPNT1 variant. The absence of the bands typical of cross β-sheets in the spectrum of 50φPNT1 (Figure 2f) enables mapping these structures to the region encompassing the first 50 residues.

2.5 | The CAR within the N-terminal α-MoRE of W^{HeV} is responsible for fibrillation

We hypothesized that the predicted CAR (^{10}GLDIID-FIQK^{19}), located within the N-terminal α-MoRE (Figure 1f) embedded within the first 50 residues region shown to be critical for fibrillation (Figure 2c), is the motif responsible for PNT1 fibrillation. To experimentally confirm its role in fibrillation, we generated a PNT1 variant in which the CAR was removed (PNT1ΔCAR variant), along with another variant in which the CAR motif was replaced with a polyalanine stretch of the same length (PNT1Ala variant) (Figure 2a). In light of the structural preferences of alanine-enriched polypeptides and as already validated in previous studies (see, e.g., Bignon et al. 2018), alanine substitution was chosen to maintain a high helical propensity within the α-MoRE. In line with expectations, though in contrast with disorder predictions that predict PNT1Ala as more disordered than PNT1 (Figure S1b), the far-UV CD spectra showed that PNT1Ala has a slightly higher α-helical content compared to PNT1 (Figure S6). Both PNT1ΔCAR and PNT1Ala variants were found to be only able to form rare amorphous aggregates that do not bind ThT (Figure 3a,b), a finding in agreement with predictions that do not identify any amyloidogenic regions within these variants (Figure S3b).

These results thus confirm the critical role of the CAR in the fibrillation process of PNT1, while ruling out the possibility that fibrillation might be merely driven by an α-helical enrichment. To assess the implication of this CAR also in the context of the full-length W^{HeV}, the first 19 residues of W^{HeV} were truncated to yield the W^{HeV}Δ19 variant. Following an oxidative pre-incubation, that is, a condition enabling W^{HeV} to form fibrils, although the W^{HeV}Δ19 variant was found to bind ThT (Figure 3c), NS-TEM showed it is unable to fibrillate, with micrographs showing only a large number of small assemblies, presumably made of disulfide-bridged oligomers (Gondelaud et al. 2024) (Figure 3d,e). The ability of W^{HeV}Δ19 to bind ThT in spite of its inability to fibrillate is consistent with our previous observations showing that ThT binding to W^{HeV} mostly reflects enhanced nucleation and does not report on fibril length (Gondelaud et al. 2024). Finally, we demonstrated the importance of the CAR by protein complementation. For

this purpose, a sample of $W^{HeV}\Delta19$, pre-incubated in oxidative conditions, was incubated for 90 min in the presence of an equimolar amount of PNT1 (Figure 3d,e). Under these conditions, a nucleation rate very similar to that of the wild-type W^{HeV} protein was observed, while PNT1 alone displays very few, though long, fibrils (Figure 3d). Measurements of fibril contour lengths showed that the fibrils length is essentially restored when $W^{HeV}\Delta19$ is incubated with PNT1 (Figure 3e). Taken together, these results confirm the key role of the CAR not only for PNT1 fibrillation but also for the full-length W^{HeV} for which it was found to be critical to enable fibril elongation from disulfide-bridged oligomers. Additionally, these results provide support for the heterotypic assembly of PNT1 and full-length W^{HeV} during fibril elongation.

2.6 | Hydrophobic residues within the CAR drive PNT1 fibrillation, while α-helicity promotes fibril nucleation

Except for the ^{10}Gly and ^{18}Gln residues, the predicted N-terminal CAR ^{10}GLDIIDFIQK^{19} is exclusively composed of nonpolar and charged residues. To decipher their role in fibrillation, the PNT1ΔPhob and PNT1ΔCharg variants were generated, where hydrophobic and charged residues, respectively, were substituted with serine residues. Serine rather than alanine was chosen to avoid jeopardizing the analysis with an alanine-driven increased α-helicity of the CAR, and also because the polar character of serine serves the dual purpose of reducing hydrophobicity and suppressing charges. In agreement with predictions (Figure S3b), PNT1ΔCharg strongly binds ThT while PNT1ΔPhob does not, suggesting that hydrophobic residues are crucial for PNT1 fibrillation (Figure 4a). Consistent with ThT measurements, no fibrils were observed on micrographs for PNT1ΔPhob (Figure 4b) confirming the critical role of the hydrophobic residues of the CAR in fibrillation. By contrast, and in a manner that could not be anticipated from predictions (Figure S3b), PNT1ΔCharg gives rise to a greatly higher number of fibrils compared to wild-type PNT1 fibrils, indicating that charged residues down-regulate fibril nucleation. The higher nucleation of PNT1ΔCharg comes at the expense of elongation, that is, PNT1ΔCharg fibrils are much shorter than fibrils formed by wild-type PNT1 (Figure 4b). Analysis of non-incubated PNT1ΔPhob and PNT1ΔCharg by CD highlighted an α-helix enrichment in PNT1ΔCharg compared to PNT1 and PNT1ΔPhob, and also a higher susceptibility to TFE (Figure 4c,d). While disorder predictions captured the lower disorder content of PNT1ΔCharg compared to PNT1ΔPhob, they failed to predict a difference between PNT1ΔCharg and PNT1 (Figure S1b).

The ability of TFE to enhance PNT1 fibril nucleation (Figure 2c) and the enrichment in α-helix of PNT1ΔCharg comfort the hypothesis of a relationship between α-helical content and fibril nucleation rate.

2.7 | The C-terminal CAR flanking region increases the aggregation kinetics of PNT1

We next assessed if the sole presence of the CAR motif is sufficient to induce PNT1 fibrillation. To this end, the CAR sequence was inserted in the 50φPNT1 variant (yielding the 50φPNT1CAR variant; Figure 2a) and the protein was analyzed as described above for the other variants. Strikingly, and in contrast with predictions (Figure S3b), 50φPNT1CAR does not bind ThT and poorly fibrillates, indicating that, beyond the CAR, additional neighboring regions contribute to fibrillation (Figure 4e,f). In further support of a role of flanking regions in fibrillation, incubation of PNT1ΔCAR with 10% TFE led to the formation of numerous, though very small, fibrils (Figure S7a). These observations advocate for a role of TFE-stabilized flanking helices in nucleation. CD spectra analysis showed that although 50φPNT1CAR exhibits a higher α-helix folding propensity compared to 50φPNT1, consistent with an inherent α-helical propensity of the CAR, it is less prone to fold compared to PNT1 (Figure 2b). These findings, which are in agreement with disorder predictions (Figure S3b), indicate that the region(s) flanking the CAR contribute(s) to the α-helical propensities of PNT1. Incubating 50φPNT1CAR with a TFE concentration as low as 5% strongly promotes ThT binding and fibrillation (Figure 4e,f), further supporting the conclusion that α-helical folding plays a role in fibrillation.

To achieve further insights into the contribution of the CAR flanking regions to PNT1 fibrillation, we focused on the regions immediately preceding or following the CAR (i.e., residues 2–9 and 20–29, respectively). Both regions fold into an α-helix, as observed in the crystal structure of the NiV N°-P complex (PDB: 4CO6) (Yabukarski et al. 2014). Two PNT1 variants were generated lacking either the N-terminal flanking α-helix (PNT1Δ9) or the C-terminal one (PNT1Δ20-29) (Figure 2a) and their fibrillation abilities were investigated (Figure 4g,h). PNT1Δ9 is still able to bind ThT and to fibrillate at an extent comparable to that of wild-type PNT1, indicating that the region spanning residues 1–9 is dispensable for PNT1 fibrillation (Figure 4g,h). Conversely, and under the same conditions, PNT1Δ20-29, albeit still able to fibrillate, exhibits a strongly decreased nucleation rate (Figure 4h) paralleled by a reduced ThT binding ability (Figure 4g). Extending the incubation time from 30 to 120 min leads to increased ThT binding and fibrillation (Figure 4g,h). These results, which could not be anticipated from amyloidogenicity predictions (Figure S3b), suggest a

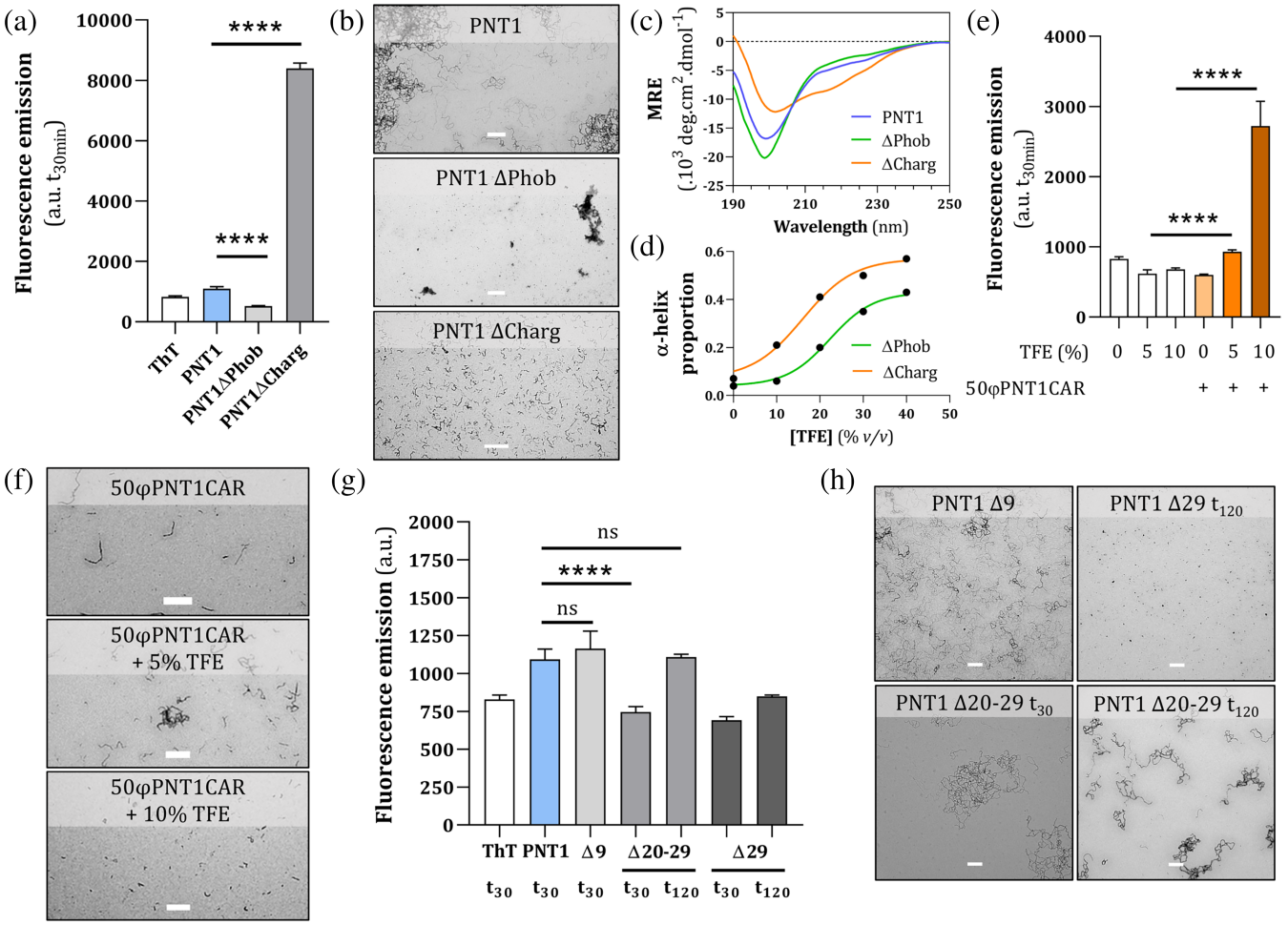

FIGURE 4 Impact of charged and hydrophobic residues of the CAR and contribution of the CAR-flanking α-helices to PNT1 fibrillation. (a) ThT fluorescence measurements after 30 min of incubation of PNT1ΔAliph and PNT1ΔCharg compared to wild-type PNT1. (b) Corresponding micrographs as obtained after 30 min of incubation. Scale bar: 500 nm. (c) CD spectra of unincubated PNT1ΔAliph and PNT1ΔCharg compared to wild-type PNT1. MRE: mean residue ellipticity. (d) Proportion of α-helix in PNT1ΔAliph and PNT1ΔCharg in the presence of 0–40% TFE as obtained from the deconvolution of CD spectra. (e) ThT fluorescence measurements after 30 min of incubation of 50φPNT1CAR in the presence of TFE (0–10%). (f) Corresponding micrographs made after 30 min of incubation. Scale bar: 500 nm. (g) ThT fluorescence measurements of PNT1, PNT1Δ9 (Δ9), PNT1Δ20-29 (Δ20-29), and PNT1Δ29 (Δ29) after 30 (t_{30}) or 120 min (t_{120}) of incubation. (h) Corresponding micrographs made at t_{30} or t_{120}. Scale bar: 500 nm. The asterisks shown in panels (a), (e), and (g) indicate a statistically significant difference ($p < 0.0001$); ns: not significant.

synergistic effect between the CAR motif and its C-terminal flanking region encompassing residues 20–29 and exhibiting strong α-helical propensities. Consistently, the removal of the CAR motif and of the 20–29 stretch (to yield PNT1Δ29) abolishes PNT1 fibrillation even at TFE concentrations as high as 30% (Figure S7b). Altogether, these results support the conclusion that although the CAR is the major driver of fibrillation, it is not sufficient to promote it, with the C-terminal flanking region endowed with α-helical propensities strongly promoting nucleation.

2.8 | The fibrillation propensity is conserved within the *Henipavirus* genus

The predicted CAR motif is part of the so-called *soyuz1* module, a conserved region encompassing the first 50 N-terminal amino acids of the phosphoprotein from members of the *Paramyxoviridae* family (Karlin and Belshaw 2012). This suggests that the V/W proteins from other henipaviruses could also undergo fibrillation. We thus generated and analyzed the PNT1 subdomain common to the P, V, and W proteins from Nipah (NiV), Mojiang (MojV), Cedar (CedV), Ghana (GhV), Langya (LyV), and Angavokely (AngV) viruses. Although CedV does not encode V/W proteins (Marsh et al. 2012), we included it in our analysis in order to improve accuracy in the determination of a consensus motif (Figure 5). Sequence alignment of the PNT1 region from the different henipaviruses revealed that the CAR motif identified in HeV PNT1 is also conserved in the other henipaviruses (Figure 5a). Analysis of this conserved motif enabled us to derive a new consensus amyloidogenic motif consisting of a glycine followed by an aliphatic residue (Φ), a polar residue ξ, an aliphatic or

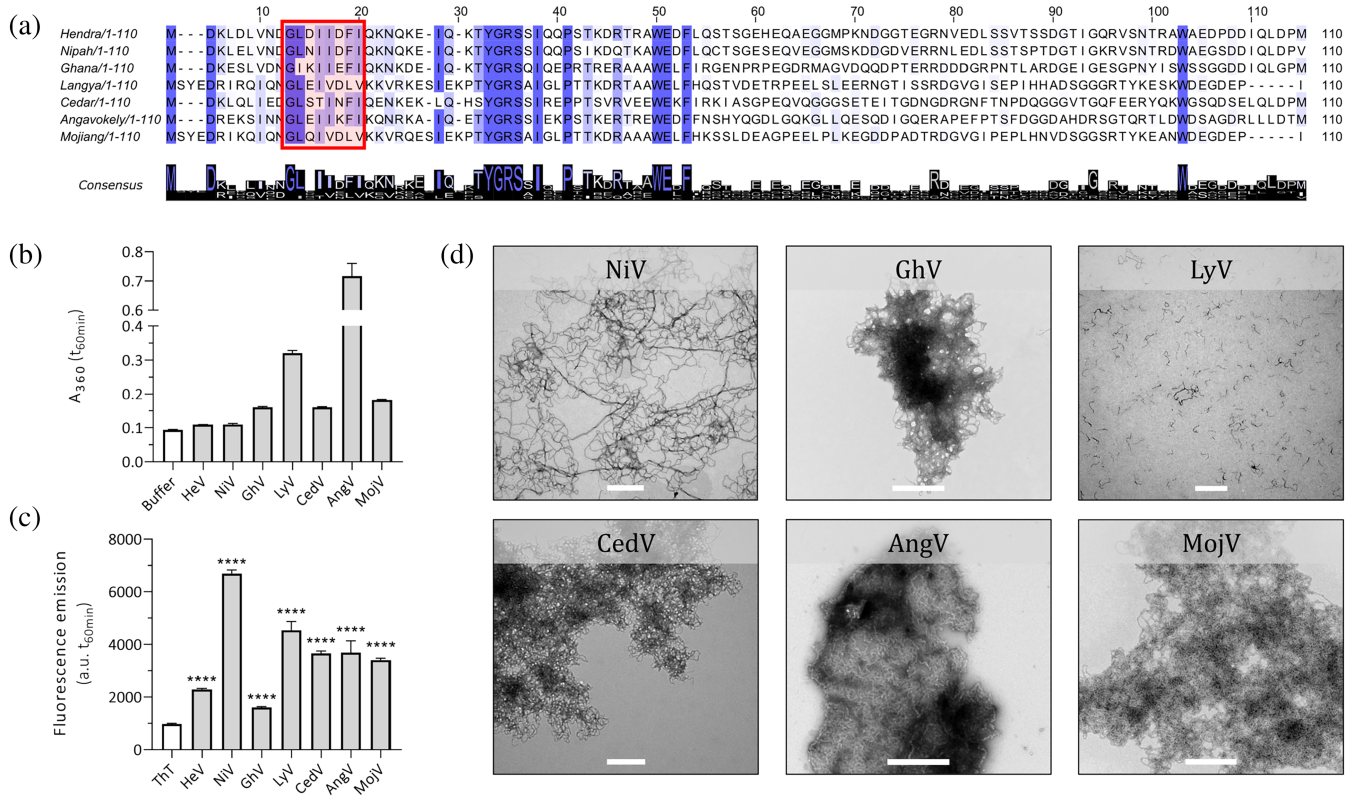

FIGURE 5 Identification of a new consensus amyloidogenic motif in the P/V/W proteins of henipaviruses and fibrillation propensities of PNT1 subdomains from various henipaviruses. (a) Sequence alignment of the 110 first amino acids (PNT1 subdomain) of the seven major *Henipavirus* P/V/W proteins, along with the derived consensus sequence, as obtained using Jalview (Procter et al. 2021). The blue gradient is related to the amino acid conservation. The identified pro-amyloidogenic motif is framed in red. Turbidity (b) and ThT fluorescence measurements (c) of the various *Henipavirus* PNT1 subdomains after 1 h of incubation ($n = 4$). The asterisks shown in panel (c) indicate a statistically significant difference ($p < 0.0001$). (d) Corresponding micrographs obtained after 1 h of incubation. Scale bar: 500 nm.

polar residue (Φ/ξ), an aliphatic residue, a polar residue, and finally a doublet made by a hydrophobic (Ψ) and an aliphatic residue (GΦξ[Φ/ξ]ΦξΨΦ motif) (Figure 5a).

The various PNT1 subdomains, which all are predicted to be disordered (Figure S1c), exhibit differences in terms of solubility (Figure 5b). These differences cannot be rationalized based on possible differences in LLPS propensities, as judged from both the absence of a correlation between MolPhase scores and measured turbidity, and the overall low predicted LLPS propensities for all these proteins (Figure S2c). Rather, differences in solubility might be related to the net charge of the first 29 amino acids (Figure S8), the pI of the rest of the polypeptide chain being similar among the various proteins.

All the PNT1 subdomains bind ThT after 1 h of incubation (Figure 5c) and form fibrillar aggregates, as observed in NS-TEM (Figure 5d). NiV PNT1 exhibits the highest ThT binding ability, which might be correlated with the ability of this protein to form fibrils that are straighter and more akin to *bona fide* amyloids (Figure 5d). Although all these proteins are predicted to be amyloidogenic (Figure S3c), the observed differences in fibrillation propensities cannot be rationalized based on predictions, as the latter identify AngV and MojV PNT1 as the most fibrillating proteins and fail to predict NiV PNT1 as the most fibrillating protein (Figure S3c).

3 | DISCUSSION

The present work originally aimed at explaining the discrepancy in the fibrillation kinetics observed between the full-length W protein from Hendra virus (Gondelaud et al. 2024; Pesce et al. 2022), and one of its subdomains, namely PNT3, that had been previously identified as a fibrillogenic region (Nilsson et al. 2022; Salladini et al. 2021). We show here that the W^{HeV} protein contains six cryptic amyloidogenic regions (CARs) distributed along the N-terminal domain (NTD) common to the P, V, and W proteins. In particular, four CARs are located within PNT3, one in PNT1 (aa 2–110) and one in PNT2 (aa 100–210). PNT1 was found to be the most fibrillogenic subdomain out of the three NTD subdomains containing CARs. We experimentally confirmed that the predicted CAR within PNT1 (residues 10–19 in

W^{HeV}) is the region responsible for the fibrillation of the whole protein, a finding implying that this CAR is endowed with the highest fibrillogenic potential out of all the six CARs predicted within the NTD of W^{HeV} (see Figure 1f). This finding is in contrast with the predicted Waltz score that predicts the CAR encompassing residues 246–255 as the most amyloidogenic (score: 93.31) and the CAR encompassing residues 10–19 as the least amyloidogenic (score: 87.16) together with the CAR spanning residues 208–214 (score: 87.05) (see http://carsdb.ppmclab.com/database/85). Although the N-terminal CAR is the main driver of PNT1 fibrillation, it is not sufficient to promote the process: fibrillation indeed also requires the C-terminal flanking region (residues 20–29). In particular, we showed that this region, known to possess inherent α-helical propensities, plays a critical role in nucleation.

The N-terminal CAR is part of a conserved P/V/W region within the *Paramyxoviridae* family, an observation that prompted us to experimentally assess and then demonstrate the fibrillogenicity of the PNT1 region from members of the *Henipavirus* genus. Based on our previous studies documenting the ability of the W^{HeV} protein to form fibrils not only *in vitro* but also *in cellula* (Gondelaud et al. 2024), it is therefore tempting to speculate, while awaiting future experimental confirmation, that all the P/V/W proteins from members of the *Henipavirus* genus might share the property of fibrillating in a cellular context.

Bioinformatic analysis of PNT1 sequences from various henipaviruses enabled us to identify a new amyloidogenic consensus motif, namely GΦξ[Φ/ξ]ΦξΨΦ. The composition of this motif, enriched in hydrophobic residues and depleted in polar and flexible residues such as proline, lysine, and arginine, is consistent with the composition of other characterized pro-amyloidogenic regions (Burdukiewicz et al. 2017).

Notably, the presence of repeated doublets of apolar residues is a characteristic shared by peptides that are able to aggregate in cross-α amyloids, as is the case of *Staphylococcus aureus* phenol-soluble modulin α3 (PSMα3 and of different synthetic peptides; Tayeb-Fligelman et al. 2017; Zhang et al. 2018). Although our experiments suggest the co-existence of both α-helices and β-sheets in fibrils, it is difficult to draw definite conclusions about the structure of the core of the fibrils without a high-resolution structure. Our ongoing efforts aimed at determining the cryo-EM structure of PNT1 fibrils will certainly provide definite answers in this regard. Nevertheless, while waiting for these high-resolution structural data to be available, a possible scenario starts to emerge. In light of our findings collectively advocating for a relationship between α-helix content and PNT1 fibrillation, and of the enrichment in cross β-sheets in fibrils, it is conceivable that the fibrillation process involves a double structural transition from a disordered to an α-helical conformation

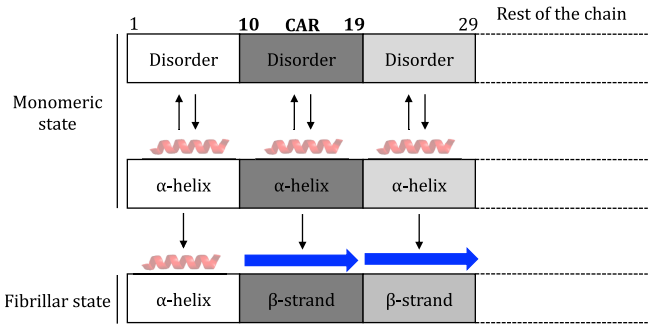

FIGURE 6 Proposed mechanism of fibrillation. The involvement of the three different N-terminal regions in the fibrillation process is depicted using a gray color gradient: the 2–9 region shown to be fully dispensable is represented in white, the CAR is shown in dark gray to reflect its role as main driver of the process, and the 20–29 region exerting a synergistic effect with the CAR and strongly promoting nucleation is shown in light gray. The α-helices are shown as partly transparent to illustrate that they are transiently populated in the unassembled form and likely also in the assembled form, contrary to the β-strands that are stabilized in the form of β-sheets in the core of the fibrils.

first, followed by an α-helix to β-strand transition that eventually leads to the formation of the cross-β-sheets found in the fibrils (Figure 6). The α-to-β switch presumably takes place within the CAR and in the C-terminal flanking region (Figure 6). In this scenario, the residual helicity observed in mature PNT1 fibrils would reflect the presence of an α-helical conformation in the flanking region(s), presumably within the 2–9 region shown to be fully dispensable for the fibrillation process. This region would not be part of the core of the fibrils and would constitute a fuzzy appendage, while the CAR and the downstream 20–29 stretch would be stabilized in the core of the amyloid fibril in the form of cross-β sheets (Figure 6). The 30–110 region would remain disordered and, together with the 2–9 region, would constitute a fuzzy coat around the fibril core.

The presence of a mixture of α-helices and β-sheets in mature fibrils may explain the relatively low ThT binding observed throughout all our experiments. Experiments with TFE and with PNT1 variants with varying degrees of α-helicity support a relationship between the α-helical content and fibril nucleation. Strikingly, this is also the case of hIAPP fibrils that are nucleated by hexamers composed of a bundle of α-helices (Sun et al. 2019; Wang et al. 2016). It is conceivable that PNT1 may similarly require an α-helix packing to be able to fibrillate. Following the nucleation stage, a transition from α-helices to β-sheets has been reported for various fibrillation mechanisms involving α-helix-rich proteins such as the amyloid-β peptide (Chen et al. 2017; Soto et al. 1995), hIAPP (Sun et al. 2019), and α-synuclein (Khammari et al. 2020), thereby providing support for our proposed mechanism.

Because the N-terminal CAR driving fibrillation is encoded by the P gene region preceding the editing

site, it does not only occur in the W protein, but it is also found in the P and V proteins. To the best of our knowledge, no evidence of P/V fibrillar aggregation has been reported so far. This inability of the P/V proteins to form fibrils might stem from the binding of the monomeric form of the nucleoprotein (N°) to the pro-amyloidogenic motif that is located within the N°-binding site, as observed in the crystal structure of the NiV N°-P complex (Yabukarski et al. 2014). This binding would lock the N-terminal region of P/V in an α-helical conformation, thereby inhibiting further self-assembly into fibrillar structures. By contrast, this inhibitory mechanism would not be at play in the case of the W protein, as, contrary to the P and V proteins that have a predominant cytoplasmic localization, it is sequestered within the nucleus of infected cells (Smith et al. 2018). In the case of NiV, a peptide encompassing residues 1–40 of P was shown to protect cells against viral infection, with this effect having been related to inhibition of N°-P complex formation (Yabukarski et al. 2014). It would be interesting to investigate the possible impairment of W fibril formation brought by this peptide, as well as to explore the antiviral potential of a shorter peptide corresponding to the pro-amyloidogenic motif we identified.

In conclusion, our study, by shedding light on the molecular mechanisms driving W^{HeV} fibril formation, enlarges our currently still limited knowledge of viral amyloids. These newly recognized amyloidogenic properties of viral proteins pave the way towards the rational design of new antiviral strategies.

4 | MATERIALS AND METHODS

4.1 | Generation of the constructs

The pDEST17 O/I expression constructs encoding the full-length W^{HeV} (UniProt P0C1C6) and W^{NiV} (UniProt P0C1C7) proteins, as well as the PNT1 (2–110), PNT2 (100–210), and PNT3 (200–310) regions of the N-terminal domain of the HeV P/V/W proteins, have been described (Gondelaud et al. 2024; Pesce et al. 2022; Salladini et al. 2021). The strategy used to generate each variant and the primers sequence used in this work are presented in Tables S1 and S2. The sequences encoding the PNT1 subdomain (residues 2–110) from Mojiang (NCBI reference sequence NC_025352.1), Cedar (NCBI Reference Sequence: YP_009094082.1), Ghana (NCBI Reference Sequence: YP_009091834.1), Langya (GenBank: UUV47243.1), and Angavokely (GenBank: UVG43983.1) viruses, optimized for expression in *E. coli*, were synthesized and subcloned in pGenDONR by Genscript (https://www.genscript.com/). The Gateway cloning technology (Thermo Fisher Scientific) was then employed for subcloning into the pDEST17 O/I vector. Constructions were sequenced (Azenta/Genewiz) and found to conform to expectations.

All constructs encode recombinant proteins in which the native sequence is preceded by a vector-encoded stretch and a TEV protease cleavage site, the latter being absent in the PNT2 and PNT3 constructs. The native amino acid sequence of all the proteins is shown in Figure S3.

4.2 | Protein expression and purification

Escherichia coli T7pRos cells were transformed and used for the expression of all the recombinant proteins. Full-length W^{HeV}, $W^{HeV}\Delta19$, and W^{NiV} proteins were expressed and purified as described in Gondelaud et al. (2024). Briefly, proteins were purified by Nickel-nitrilotriacetic acid (Ni-NTA) affinity chromatography (Cytiva) and anion-exchange chromatography (Diethylaminoethyl, DEAE, resin, Cytiva) under denaturing conditions (6M urea). Eluted fractions were reduced by the addition of 5 mM DTT and incubated for 30 min on ice. DTT was then removed using a HiPrep desalting column (Cytiva) and the resulting samples, containing monomeric species, were stored at −80°C in the presence of 6M urea.

For HeV PNT subdomains and PNT1 variants, starting from a 100-mL preculture in lysogeny broth (LB) medium containing 100 μg/mL ampicillin and 34 μg/mL chloramphenicol grown overnight (O/N) at 37°C and 200 rpm, 1.5 L of terrific broth (TB) was inoculated and incubated at 25°C and at 200 rpm O/N. Induction was carried out with 1 mM isopropyl β-D-1-thiogalactopyranoside (IPTG) for 3 h at 25°C. Cultures were then centrifuged at 6000*g* for 10 min, 10°C and the pellets resuspended in 40–50 mL of HBS/Urea buffer containing 20 mM HEPES pH 7.2, 150 mM NaCl, 6M urea. Cells were lysed by sonication for 5 min at 500 W. Lysates were then centrifuged at 15,000*g* for 30 min, 4°C and the supernatant was added to 2 mL of Ni-NTA agarose beads (Cytiva) and incubated with gentle agitation (15 rpm) for 45 min at 4°C. The resin was then washed by 25 volumes of washing buffer (HBS/Urea buffer containing 1M NaCl) and proteins were then eluted with desalting buffer (20 mM HEPES pH 7.2, 50 mM NaCl, 6M urea) supplemented with 0.5M imidazole.

Eluates from Ni-NTA affinity chromatography were further purified by anion-exchange chromatography using a DEAE column (Cytiva) pre-equilibrated in desalting buffer. Proteins were eluted with 20 mM HEPES pH 7.2, 500 mM NaCl, and 6M urea. The fractions of interest were pooled, concentrated with an amicon ultra centrifugal filter with a molecular mass cutoff of 10 kDa (Merck Millipore) and injected onto a HiLoad Superdex 75 pg 16/600 gel filtration column (Cytiva) and eluted in HBS/Urea buffer. Proteins were then

concentrated as described above and stored at −80°C. In the case of PNT2, which contains a cysteine residue, 10 mM DTT was added to the eluted fractions obtained from both Ni-NTA affinity and gel filtration chromatography. DTT was then removed by injecting the reduced and purified PNT2 onto a HiPrep desalting column (Cytiva) in HBS/Urea buffer prior to storage at −80°C.

Protein concentrations were estimated using the theoretical absorption coefficients at 280 nm as obtained using the program ProtParam from the EXPASY server (Wilkins et al. 1999).

4.3 | Protein aggregation, turbidimetry, and thioflavin T fluorescence measurements

The same protocol described in Gondelaud et al. (2024) was followed. Five-hundred microliters at a concentration of 75 μM (W^{HeV} and W^{NiV}) or 100 μM (NTD subdomains) were desalted in urea-free buffer (HBS) using a PD Minitrap G-25 column (Cytiva). The resulting urea-free protein samples were analyzed at a final concentration of 30 μM (W^{HeV} and W^{NiV}) or 40 μM (NTD subdomains) in the presence of 50 μM thioflavin T. For some experiments, W^{HeV} and $W^{HeV}\Delta19$ were pre-incubated in denaturing conditions (HBS/urea) for 48 h as detailed in Gondelaud et al. (2024) in order to promote the formation of disulfide bonds required for fibrillation. The protein complementation experiment between PNT1 and $W^{HeV}\Delta19$ was carried out as follows: a sample containing 25 μM of $W^{HeV}\Delta19$ pre-incubated in oxidative condition for 48 h was mixed with 25 μM of PNT1 in urea-free buffer, and the mixture was incubated for 90 min at 37°C before NS-TEM grid preparation. For experiments carried out in the presence of TFE, the latter was directly added after urea removal. Turbidity measurements were made at 360 nm, and fluorescence measurements were performed on a Tecan microplate reader GENios Plus in black 96-well plates with transparent flat bottoms (Greiner, 655096). ThT was excited at 430 nm, and fluorescence emission was recorded at 535 nm. Measurements were performed at least in quadruplicate (the precise number being indicated in each experiment) and data are represented as mean ± standard deviation (SD). Statistical analysis was performed using a Student's *t* test.

4.4 | Circular dichroism

Far-UV circular dichroism (CD) spectra were acquired using a Jasco J-810 (Japan) flushed with 10 L/min gaseous N_2 and equipped with a Peltier and a water temperature control system set to 20°C. Proteins, incubated or not, were analyzed at a final concentration of 4 μM (W^{HeV}) or 10 μM (NTD subdomains) in 10 mM sodium phosphate pH 7.2 in a 1-mm-thick quartz cuvette. Five spectra, acquired between 260 and 190 nm, were buffer-subtracted and averaged. For experiments with TFE, the osmolyte was added to urea-free protein samples right before CD spectra acquisitions at final concentrations varying from 0 to 50% (v/v) as detailed in the text. The content in secondary structures was determined by deconvolution using the Dichroweb server (Miles et al. 2022). The CDSSTR deconvolution algorithm was used for this purpose with the reference proteins data set 7.

4.5 | Fourier transform infrared spectroscopy

HeV PNT1 and 50φPNT1 were incubated for 1 h at 37°C at a final concentration of 40 μM and then lyophilized overnight. Samples were then resuspended to a final concentration of 150 μM in deuterated water and incubated at 4°C for 48 h. Fifty microliter of each sample was placed between two CaF_2 windows separated by a 50-μm Teflon film spacer. This liquid cell was then placed in a thermostated cell holder, and transmission IR spectra were recorded on a Jasco™ FT/IR 6100 spectrometer equipped with a triglycine sulfate (TGS) detector. The interferometer and the sample chamber were continuously purged with dry air. All the spectra were an average of 128 scans, with 4 cm^{-1} of resolution, from 4000 to 400 cm^{-1}, apodized with a cosine function. Subtractions and Fourier self-deconvolutions were performed using the Spectra Manager™ software. Buffer was subtracted using an offset between 1850 and 2000 cm^{-1}. All spectra were corrected for the presence of water vapor. Local baseline correction was performed in order to normalize slight differences at analyzed spectral bands. The analysis was focused on the protein amide I′ (Susi and Byler 1986). Amide I′ bands (1700–1600 cm^{-1}) are presented.

4.6 | Negative-staining electron microscopy

Proteins samples were diluted in HBS at a final concentration of 2 μM (W proteins) or 4 μM (NTD subdomains). Grids were prepared as follows: carbon-coated grids (Carbon 300 mesh 3 mm Cu, TAAB) were exposed to plasma glow discharge for 20 s using a GloQube (Quorum) with a current of 25 mA. A sample volume of 3.5 μL was deposited on the grid for a minute, then blotted and washed three times in HBS before being incubated with 35 μL of 1% (w/v) uranyl acetate solution for a minute. Grids were then blotted and dried overnight before being observed on a TECNAI T12 Spirit microscope (Thermo Company) operated at 120 kV equipped with a Veleta 2Kx2K CCD camera

(Olympus). Measurements of the fibrils contour length were made using the ImageJ software (Schneider et al. 2012) by manually tracing the fibers observed on micrographs.

4.7 | Bioinformatics analysis

CARs were retrieved from the CAR database (Pintado-Grima et al. 2022). The CAR database contains pre-computed predictions for all pro-aggregating regions present in the disordered proteins deposited in the DisProt database (Aspromonte et al. 2023). Disorder predictions were carried out using the Multilayered Fusion-based Disorder predictor (MFDp) (http://biomine.cs.vcu.edu/servers/MFDp/) (Mizianty et al. 2010). This metapredictor combines the results from multiple complementary disorder predictors, namely DISOclust, DISOPRED, IUPRED-L, and IUPRED-S, while also taking into account secondary structure predictions and solvent accessibility to generate its consensus.

Prediction of amyloidogenic regions was carried out using the FoldAmyloid server (http://bioinfo.protres.ru/fold-amyloid/) (Garbuzynskiy et al. 2010) and default parameters. Predictions of propensities to undergo LLPS were obtained using the MolPhase predictor (http://molphase.sbs.ntu.edu.sg/) (Liang et al. 2024).

The first 110 amino acid residues of the P/V/W proteins from Hendra, Nipah, Mojiang, Cedar, Ghana, Langya, and Angavokely viruses were aligned using T-Coffee (Di Tommaso et al. 2011) and their sequence was analyzed with Jalview (Procter et al. 2021). Isoelectric points were calculated using ProtParam (Wilkins et al. 1999). Secondary structure predictions were obtained using JPRED4 (Drozdetskiy et al. 2015).

AUTHOR CONTRIBUTIONS

Frank Gondelaud: Conceptualization; investigation; writing – original draft; validation; writing – review and editing; formal analysis; supervision. **Christophe Bignon:** Investigation; writing – review and editing. **Denis Ptchelkine:** Investigation; writing – review and editing. **Frédéric Carrière:** Investigation; writing – review and editing; formal analysis. **Sonia Longhi:** Conceptualization; funding acquisition; writing – review and editing; project administration; supervision.

ACKNOWLEDGMENTS

We thank Cyrille Mathieu, Denis Gerlier, and Alexandre Lalande (CIRI, Lyon, France) for useful comments on the studies herein presented, as well as Moulay Sahaka (BIP Laboratory) for technical assistance regarding FTIR analysis. We thank all the AFMB technical and support staff (Denis Patrat, Patricia Clamecy, Béatrice Rolland, Chantal Falaschi, and Fabienne Amalfitano). This work was carried out with the financial support of the Agence Nationale de la Recherche (ANR), specific project Heniphase (ANR-21-CE11-0012-01). The Heniphase project is labeled by the Eurobiomed Pôle de Compétitivité. This project was also partly supported by the French Infrastructure for Integrated Structural Biology (FRISBI) (ANR-10-INSB-0005) and by the CNRS. F.G. was supported by a post-doctoral fellowship from the FRM (Fondation pour la Recherche Médicale) and by the FRM specific project MND202310017898. The funders had no role in the design of the study; in the collection, analyses, or interpretation of data; in the writing of the manuscript; or in the decision to publish the results. A CC-BY public copyright license has been applied by the authors to the present document and will be applied to all subsequent versions up to the author accepted manuscript arising from this submission, in accordance with the grant's open access conditions.

DATA AVAILABILITY STATEMENT

The data that support the findings of this study are available from the corresponding author upon reasonable request.

ORCID

Sonia Longhi https://orcid.org/0000-0002-6829-6771

REFERENCES

Alberti S, Hyman AA. Biomolecular condensates at the nexus of cellular stress, protein aggregation disease and ageing. Nat Rev Mol Cell Biol. 2021;22:196–213.

Aspromonte MC, Nugnes MV, Quaglia F, Bouharoua A, DisProt Consortium, Tosatto SCE, et al. DisProt in 2024: improving function annotation of intrinsically disordered proteins. Nucleic Acids Res. 2023;52:D434–41.

Audsley MD, Moseley GW. Paramyxovirus evasion of innate immunity: diverse strategies for common targets. World J Virol. 2013;2:57–70.

Basler CF. Nipah and Hendra virus interactions with the innate immune system. Curr Top Microbiol Immunol. 2012;359:123–52.

Bignon C, Troilo F, Gianni S, Longhi S. Partner-mediated polymorphism of an intrinsically disordered protein. J Mol Biol. 2018;430:2493–507.

Brocca S, Grandori R, Longhi S, Uversky V. Liquid-liquid phase separation by intrinsically disordered protein regions of viruses: roles in viral life cycle and control of virus-host interactions. Int J Mol Sci. 2020;21:9045.

Burdukiewicz M, Sobczyk P, Rödiger S, Duda-Madej A, Mackiewicz P, Kotulska M. Amyloidogenic motifs revealed by n-gram analysis. Sci Rep. 2017;7:12961.

Chen G, Xu T, Yan Y, Zhou Y, Jiang Y, Melcher K, et al. Amyloid beta: structure, biology and structure-based therapeutic development. Acta Pharmacol Sin. 2017;38:1205–35.

Di Tommaso P, Moretti S, Xenarios I, Orobitg M, Montanyola A, Chang J-M, et al. T-Coffee: a web server for the multiple sequence alignment of protein and RNA sequences using structural information and homology extension. Nucleic Acids Res. 2011;39:W13–7.

Drozdetskiy A, Cole C, Procter J, Barton GJ. JPred4: a protein secondary structure prediction server. Nucleic Acids Res. 2015;43:W389–94.

Erdős G, Dosztányi Z. Analyzing protein disorder with IUPred2A. Curr Protoc Bioinformatics. 2020;70:e99.
Escudero-Pérez B, Lalande A, Mathieu C, Lawrence P. Host–pathogen interactions influencing zoonotic spillover potential and transmission in humans. Viruses. 2023;15:599.
Garbuzynskiy SO, Lobanov MY, Galzitskaya OV. FoldAmyloid: a method of prediction of amyloidogenic regions from protein sequence. Bioinformatics. 2010;26:326–32.
Gazal S, Sharma N, Gazal S, Tikoo M, Shikha D, Badroo GA, et al. Nipah and Hendra viruses: deadly zoonotic paramyxoviruses with the potential to cause the next pandemic. Pathogens. 2022; 11:1419.
Glon D, Léonardon B, Guillemot A, Albertini A, Lagaudrière-Gesbert C, Gaudin Y. Biomolecular condensates with liquid properties formed during viral infections. Microbes Infect. 2024; 26:105402.
Gondelaud F, Lalande A, Pesce G, Bignon C, Fourquet P, Ptchelkine D, et al. Redox-dependent formation of a viral amyloid and functional impact. 2024. Available from: https://www.biorxiv.org/content/10.1101/2024.01.22.576663v1
Gondelaud F, Leval J, Arora L, Walimbe A, Bignon C, Ptchelkine D, et al. Unraveling the molecular grammar and the structural transitions underlying the fibrillation of a viral fibrillogenic domain. Protein Sci. 2025; 34:e70068.
Gondelaud F, Lozach P-Y, Longhi S. Viral amyloids: new opportunities for antiviral therapeutic strategies. Curr Opin Struct Biol. 2023;83:102706.
Gondelaud F, Pesce G, Nilsson JF, Bignon C, Ptchelkine D, Gerlier D, et al. Functional benefit of structural disorder for the replication of measles, Nipah and Hendra viruses. Essays Biochem. 2022; 66:915-34.
Habchi J, Mamelli L, Darbon H, Longhi S. Structural disorder within Henipavirus nucleoprotein and phosphoprotein: from predictions to experimental assessment. PLoS One. 2010;5:e11684.
Isaacs A, Low YS, Macauslane KL, Seitanidou J, Pegg CL, Cheung STM, et al. Structure and antigenicity of divergent Henipavirus fusion glycoproteins. Nat Commun. 2023;14:3577.
Jansen R, Grudzielanek S, Dzwolak W, Winter R. High pressure promotes circularly shaped insulin amyloid. J Mol Biol. 2004;338: 203–6.
Jensen MR, Yabukarski F, Communie G, Condamine E, Mas C, Volchkova V, et al. Structural description of the Nipah virus phosphoprotein and its interaction with STAT1. Biophys J. 2020; 118:2470–88.
Karlin D, Belshaw R. Detecting remote sequence homology in disordered proteins: discovery of conserved motifs in the N-termini of Mononegavirales phosphoproteins. PLoS One. 2012;7:e31719.
Kaza B, Aguilar HC. Pathogenicity and virulence of henipaviruses. Virulence. 2023;14:2273684.
Keiffer TR, Ciancanelli MJ, Edwards MR, Basler CF. Interactions of the Nipah virus P, V, and W proteins across the STAT family of transcription factors. mSphere. 2020;5:e00449-20.
Khammari A, Arab SS, Ejtehadi MR. The hot sites of α-synuclein in amyloid fibril formation. Sci Rep. 2020;10:12175.
Li H, Kim J-YV, Pickering BS. Henipavirus zoonosis: outbreaks, animal hosts and potential new emergence. Front Microbiol. 2023; 14:1167085.
Liang Q, Peng N, Xie Y, Kumar N, Gao W, Miao Y. MolPhase, an advanced prediction algorithm for protein phase separation. EMBO J. 2024;43:1898–918.
Madera S, Kistler A, Ranaivoson HC, Ahyong V, Andrianiaina A, Andry S, et al. Discovery and genomic characterization of a novel Henipavirus, Angavokely virus, from fruit bats in Madagascar. J Virol. 2022;96:e0092122.
Marsh GA, de Jong C, Barr JA, Tachedjian M, Smith C, Middleton D, et al. Cedar virus: a novel Henipavirus isolated from Australian bats. PLoS Pathog. 2012;8:e1002836.
Miles AJ, Ramalli SG, Wallace BA. DichroWeb, a website for calculating protein secondary structure from circular dichroism spectroscopic data. Protein Sci. 2022;31:37–46.
Milles S, Jensen MR, Lazert C, Guseva S, Ivashchenko S, Communie G, et al. An ultraweak interaction in the intrinsically disordered replication machinery is essential for measles virus function. Sci Adv. 2018;4:eaat7778.
Mizianty MJ, Stach W, Chen K, Kedarisetti KD, Disfani FM, Kurgan L. Improved sequence-based prediction of disordered regions with multilayer fusion of multiple information sources. Bioinformatics. 2010;26:i489–96.
Natalello A, Ami D, Doglia SM. Fourier transform infrared spectroscopy of intrinsically disordered proteins: measurement procedures and data analyses. Methods Mol Biol. 2012;895:229–44.
Nilsson JF, Baroudi H, Gondelaud F, Pesce G, Bignon C, Ptchelkine D, et al. Molecular determinants of fibrillation in a viral amyloidogenic domain from combined biochemical and biophysical studies. Int J Mol Sci. 2022;24:399.
Pesce G, Gondelaud F, Ptchelkine D, Bignon C, Fourquet P, Longhi S. Dissecting Henipavirus W proteins conformational and fibrillation properties: contribution of their N- and C-terminal constituent domains. FEBS J. 2024;292:556–81.
Pesce G, Gondelaud F, Ptchelkine D, Nilsson JF, Bignon C, Cartalas J, et al. Experimental evidence of intrinsic disorder and amyloid formation by the Henipavirus W proteins. Int J Mol Sci. 2022;23:923.
Pintado-Grima C, Bárcenas O, Manglano-Artuñedo Z, Vilaça R, Macedo-Ribeiro S, Pallarès I, et al. CARs-DB: a database of cryptic amyloidogenic regions in intrinsically disordered proteins. Front Mol Biosci. 2022;9:882160.
Piracha ZZ, Saeed U, Ahmed RA, Khan FN, Nasir MI. Global emergence of Langya virus: a serious public health concern. J Glob Health. 2023;13:03034.
Procter JB, Carstairs GM, Soares B, Mourão K, Ofoegbu TC, Barton D, et al. Alignment of biological sequences with Jalview. Methods Mol Biol. 2021;2231:203–24.
Quarleri J, Galvan V, Delpino MV. Henipaviruses: an expanding global public health concern? GeroScience. 2022;44:1–13.
Receveur-Bréchot V, Bourhis J-M, Uversky VN, Canard B, Longhi S. Assessing protein disorder and induced folding. Proteins. 2006; 62:24–45.
Salladini E, Delauzun V, Longhi S. The Henipavirus V protein is a prevalently unfolded protein with a zinc-finger domain involved in binding to DDB1. Mol Biosyst. 2017;13:2254–67.
Salladini E, Gondelaud F, Nilsson JF, Pesce G, Bignon C, Murrali MG, et al. Identification of a region in the common amino-terminal domain of Hendra virus P, V, and W proteins responsible for phase transition and amyloid formation. Biomolecules. 2021;11:1324.
Schiavina M, Salladini E, Murrali MG, Tria G, Felli IC, Pierattelli R, et al. Ensemble description of the intrinsically disordered N-terminal domain of the Nipah virus P/V protein from combined NMR and SAXS. Sci Rep. 2020;10:19574.
Schneider CA, Rasband WS, Eliceiri KW. NIH image to ImageJ: 25 years of image analysis. Nat Methods. 2012;9:671–5.
Schramm A, Bignon C, Brocca S, Grandori R, Santambrogio C, Longhi S. An arsenal of methods for the experimental characterization of intrinsically disordered proteins—How to choose and combine them? Arch Biochem Biophys. 2019;676:108055.
Schramm A, Lieutaud P, Gianni S, Longhi S, Bignon C. InSiDDe: a server for designing artificial disordered proteins. Int J Mol Sci. 2017;19:91.
Smith KM, Tsimbalyuk S, Edwards MR, Cross EM, Batra J, Soares da Costa TP, et al. Structural basis for importin alpha 3 specificity of W proteins in Hendra and Nipah viruses. Nat Commun. 2018; 9:3703.
Soto C, Castaño EM, Frangione B, Inestrosa NC. The alpha-helical to beta-strand transition in the amino-terminal fragment of the

amyloid beta-peptide modulates amyloid formation. J Biol Chem. 1995;270:3063–7.
Sun Y, Kakinen A, Xing Y, Faridi P, Nandakumar A, Purcell AW, et al. Amyloid self-assembly of hIAPP8-20 via the accumulation of helical oligomers, α-helix to β-sheet transition, and formation of β-barrel intermediates. Small. 2019;15:e1805166.
Susi H, Byler DM. Resolution-enhanced Fourier transform infrared spectroscopy of enzymes. Methods Enzymol. 1986;130:290–311.
Tayeb-Fligelman E, Tabachnikov O, Moshe A, Goldshmidt-Tran O, Sawaya MR, Coquelle N, et al. The cytotoxic *Staphylococcus aureus* PSMα3 reveals a cross-α amyloid-like fibril. Science. 2017;355:831–3.
Wang L, Ilitchev AI, Giammona MJ, Li F, Buratto SK, Bowers MT. Human islet amyloid polypeptide assembly: the key role of the 8-20 fragment. J Phys Chem B. 2016;120:11905–11.
Wilkins MR, Gasteiger E, Bairoch A, Sanchez JC, Williams KL, Appel RD, et al. Protein identification and analysis tools in the ExPASy server. Methods Mol Biol. 1999;112:531–52.
Yabukarski F, Lawrence P, Tarbouriech N, Bourhis J-M, Delaforge E, Jensen MR, et al. Structure of Nipah virus unassembled nucleoprotein in complex with its viral chaperone. Nat Struct Mol Biol. 2014;21:754–9.
Zhang S-Q, Huang H, Yang J, Kratochvil HT, Lolicato M, Liu Y, et al. Designed peptides that assemble into cross-α amyloid-like structures. Nat Chem Biol. 2018;14:870–5.

SUPPORTING INFORMATION

Additional supporting information can be found online in the Supporting Information section at the end of this article.

How to cite this article: Gondelaud F, Bignon C, Ptchelkine D, Carrière F, Longhi S. A conserved motif in *Henipavirus* P/V/W proteins drives the fibrillation of the W protein from Hendra virus. Protein Science. 2025;34(4):e70085. https://doi.org/10.1002/pro.70085